

# Deformation analysis of reinforced-core auxetic assemblies by close-range photogrammetry

Igor Shufrin<sup>\*1,2</sup>, Elena Pasternak<sup>\*\*1</sup>, and Arcady V. Dyskin<sup>\*\*\*2</sup>

<sup>1</sup> School of Mechanical and Chemical Engineering, The University of Western Australia, 35 Stirling Highway, WA, Crawley 6009, Australia

<sup>2</sup> School of Civil Environmental and Mining Engineering, The University of Western Australia, 35 Stirling Highway, WA, Crawley 6009, Australia

Received 18 November 2015, revised 11 April 2016, accepted 3 May 2016

Published online 20 June 2016

**Keywords** auxetics, close-range photogrammetry, rapid prototyping, reinforced-core units

\* Corresponding author: e-mail igor.shufrin@uwa.edu.au, Phone: +61 8 6488 8518, Fax: +61 8 6488 1024

\*\* e-mail elena.pasternak@uwa.edu.au

\*\*\* e-mail arcady.dyskin@uwa.edu.au

In this article, we present an experimental study validating the concept of the reinforced-core auxetic assemblies. The main distinctive feature of these assemblies is the presence of a reinforcing core in the microstructural units that increases the shear stiffness and thus produces negative Poisson's ratio. We tested a number of prototypes manufactured using the stereolithography and selective laser sintering methods. To measure the deformations, we employed the close-range photogrammetry method, which enables monitoring of locations of unlimited number of points from digital images.

We developed a procedure for multi-point measurement of planar deformations using a single digital camera. This procedure allows for continuous measurement of deformations without interruption to the loading sequence. Camera self-calibration is based on multiple images of stable reference points, which enables high accuracy of the measurements even using a consumer grade digital camera. We compare the obtained experimental results with a simplified continuum model. We demonstrate a good agreement between the theoretical predictions and the experimental results.

© 2016 WILEY-VCH Verlag GmbH & Co. KGaA, Weinheim

**1 Introduction** Auxetic materials are materials with microstructure engineered in such a way that they exhibit negative Poisson's ratio at the macroscopic level. In particular, such materials contract laterally when compressed longitudinally. Although, this kind of behaviour is thermodynamically permitted, in nature the negative Poisson's ratio is only observed in some crystals in certain directions [1–6] that is in highly anisotropic materials. The first man-made auxetic material reported in the literature was a foam with re-entrant cells that unfolded when stretched [7]. Since then the intensive research in the area of auxetics has identified a number of auxetic systems consisting of re-entrant honeycomb structures [7–9], tethered-nodule networks [10–12], chiral systems [13–17], rotating rigid and semi-rigid units [18–22], interlocking units [23, 24], granular materials [24–26], various molecular models [8, 27–33], foldable microstructures [34], foams

with missing ribs [35], perforated sheets [36–40], materials with cracks with suppressed shearing [41], auxetic lattices [42, 43], beam and pivots networks [44], multiphase composites with re-entrant microstructure [45, 46], multi-layered composites [47] and hollow sphere stacks [48].

Despite the variety of auxetic systems presented in the literature, manufacture of auxetic materials still remains a challenge. Several manufacturing routes have been proposed to convert a conventional (positive Poisson's ratio) foam into the auxetic one using heat treatment, thermoforming and compaction [49–53]. The main approaches used for experimental manufacturing of auxetics are based on the rapid prototyping techniques such as the soft lithography [54], the selective electron beam melting [55, 56], the digital micromirror device projection printing [57] and the dip-in direct laser writing [58]. Other kinds of auxetic systems that were fabricated included

auxetic textile [59], sandwich structures with auxetic core [60] and auxetic composites [16, 61]. The latest developments in the area of auxetics have been presented in the recent reviews of Greaves et al. [62], Prawoto [63], and Carneiro et al. [64] and a monograph of Lim [65].

The peculiar behaviour of auxetic materials leads to several unusual properties and interesting types of mechanical behaviour, such as amplified shear moduli [64–66], a decrease in thermal stresses [41, 67], increased indentation resistance [68–70], superior pullout resistance [71], shape memory effects [72] and synclastic behaviour [68, 73]. These properties create prompt new applications of auxetic materials such as auxetic stents [74], auxetic textile [59, 75], auxetic fasteners [64] and deployable structures [76]. The auxetic materials have a great potential in design of piezoceramic composites [54, 63, 68], auxetic sensors [66] and smart structures with tuneable behaviour [72, 77–79].

Recently, we proposed a novel concept for design of microstructures exhibiting negative Poisson's ratio on the macroscopic level [26]. The main distinctive feature of this concept is the introduction of a reinforcing core into each periodic unit that increases the resistance to shear deformations. These structures have hexagonal (sixfold) symmetry, which produces elastic isotropy in the plane perpendicular to the axis of the hexagonal symmetry. Using several modelling techniques, we showed that these isotropic systems are able to provide the Poisson's ratio as low as  $-0.9$  [26].

In this article, we focus on the experimental verification of the concept of the reinforced-core isotropic auxetic assemblies. We report the results of experiments conducted on a number of prototypes manufactured using stereolithography and selective laser sintering methods. To measure the deformations, we employ the close-range photogrammetry method, which enables monitoring of the deformations at any number of points. We derive a procedure to analyse the strain developing in the plane of the prototype using a single digital camera. This measuring procedure does not require loading interruptions; the number of measurements (images) is only limited by the speed of the camera. We use a special series of images for camera self-calibration, which enables high accuracy of the measurements even using a semi-metric consumer (off-the-shelf) camera. We compare the obtained experimental results with the finite element and structural analyses of the prototypes and with the continuum model of a general assembly. We demonstrate that the experimental results validate the theoretical predictions.

The article is structured as follows. Section 2 introduces the reinforced-core auxetic systems. In essence, we consider a macroscopic material whose microstructure is such that leads to a negative macroscopic Poisson's ratio. We use a homogenisation procedure to evaluate the type of its behaviour needed to produce the macroscopic auxeticity. We physically construct a representative cell that will show that under available type of loading it produces desired auxetic

behaviour. We present the prototypes manufactured using the rapid prototyping techniques and develop numerical models for analysis of these prototypes. Section 3 presents the experimental investigation procedure of the auxetic microstructure. We describe the experimental setup and the photogrammetric procedure we developed for non-contact measurement of planar deformation enabling the evaluation of Poisson's ratio. Section 4 analyses the experimental results and compares them with the theoretical developments.

## 2 Reinforced core hexagonal auxetic assemblies

The proposed design concept is based on the fact that Poisson's ratio of  $-1$  corresponds to the case when the deviatoric strain is negligible. In isotropic materials, it follows that the Young's modulus is negligible compared to the shear modulus. Therefore, if a microstructure is to exhibit macroscopic negative Poisson's ratio it should be constructed from elements that prevent the angle change or shear along with the low resistance to volumetric deformation [79, 80]. Alternatively, if the microstructural elements do not exhibit this property the shear connection between the elements should be considerably stiffer than the normal one [25, 26, 81]. In our previous work, we applied these ideas to develop an isotropic microstructure that yields negative macroscopic Poisson's ratio [26]. Here we recall the main ideas of this approach and present the rapid prototyping models along with a set of simulation methods used for their analysis.

### 2.1 Design of macroscopic isotropic auxetic materials

The design of auxetic materials that we present in this study capitalises on the concept of meta-materials, in which the auxetic material is constructed from conventional materials and the negative Poisson's ratio is only obtained as a macroscopic property by averaging the stress–strain relations over suitable large volume elements. As a result, there are always two scales involved: the microscopic scale representing the internal structure and the macroscopic scale exhibiting the effective properties of the meta-material. Note that we call these scales micro- and macroscopic irrespective of the actual size of the structure. In modelling, the transition between these scales is achieved by homogenisation, the mathematical procedure yielding a continuum description of the material [41].

Here we employ the homogenisation procedure developed in Refs. [82–84] for the continuum description of granular materials. This procedure treats the microstructure as an assembly of rigid units connected by a set of linear elastic springs. It was demonstrated that the required macroscopic characteristics of the assembly can be constructed by controlling the stiffness of these connections [26, 41, 48, 80, 85]. The detailed derivations of this procedure that defines the Cosserat constitutive relations for an arbitrary assembly of rigid particles are outlined in Appendix A.

For the particular case treated in this study, we consider a close-pack planar assembly of identical microstructural

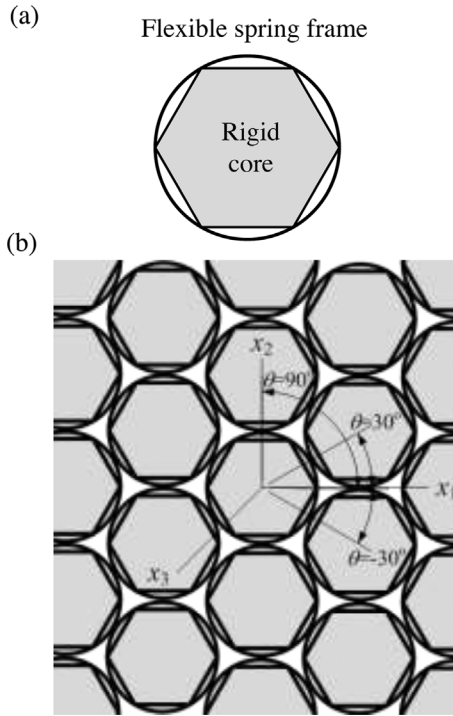


**Figure 1** Reinforced-core isotropic auxetic assembly: (a) reinforced-core unit, (b) regular hexagonal assembly.

units that possesses a six-order hexagonal symmetry shown in Fig. 1b. This arrangement ensures that macroscopically such material exhibiting isotropic properties in the plane of the assembly [26, 86]. In this hexagonal assembly, each unit has three identical pairs of connectors. Each pair consists of two connectors symmetrically located at the opposite sides of the microstructural unit. In 2D, each connection can be described using three linear springs: translational springs in the normal and tangential directions and a rotational spring. The normal spring characterised by stiffness  $k_n$  acts along the line connecting the centres of the contacting units. The tangential (shear) spring of stiffness  $k_s$  is oriented perpendicular to the normal one and acts in the plane of the assembly. The rotational spring of stiffness  $k_\phi$  resists relative rotations (about the axis normal to the plane of the assembly) between two neighbouring units. Following the homogenisation procedure detailed in Appendix A, we define three connections oriented as [26, 48] (cf. Fig. 1b)

$$\theta = 30^\circ; \psi = 0 \quad (1a)$$

$$\theta = 90^\circ; \psi = 0 \quad (1b)$$

$$\theta = -30^\circ; \psi = 0. \quad (1c)$$

The presence of independent mutual rotations resisted by the rotational springs calls for the use of a 2D Cosserat continuum, see Appendix A. The constitutive relations of

the equivalent 2D Cosserat continuum were obtained in [26, 48, 87–91]. They read:

$$\sigma_{11} = \frac{\sqrt{3}}{4h} ((3k_n + k_s)\gamma_{11} + (k_n - k_s)\gamma_{22}) \quad (2a)$$

$$\sigma_{12} = \frac{\sqrt{3}}{4h} ((k_n + 3k_s)\gamma_{12} + (k_n - k_s)\gamma_{21}) \quad (2b)$$

$$\sigma_{21} = \frac{\sqrt{3}}{4h} ((k_n - k_s)\gamma_{12} + (k_n + 3k_s)\gamma_{21}) \quad (2c)$$

$$\sigma_{22} = \frac{\sqrt{3}}{4h} ((k_n - k_s)\gamma_{11} + (3k_n + k_s)\gamma_{22}) \quad (2d)$$

$$\mu_{13} = \frac{\sqrt{3}}{h} k_\phi \kappa_{13} \quad (2e)$$

$$\mu_{23} = \frac{\sqrt{3}}{h} k_\phi \kappa_{23} \quad (2f)$$

where  $\gamma_{ij}$  and  $\chi_{ij}$  are the Cosserat strain and curvature defined in Eqs. (A.6) and (A.7),  $\sigma_{ij}$  and  $\mu_{ij}$  are the Cosserat (non-symmetric) stress and couple stress, see Eqs. (A.8), and  $h$  is the thickness of the assembly.

Comparing Eqs. (2) to the constitutive equations for 2D isotropic Cosserat continuum [92], we derive the expressions for the Young's modulus,  $E$ , shear modulus,  $G$ , Poisson's ratio,  $\nu$ , and two combined Cosserat moduli  $\alpha$  and  $\gamma + \varepsilon$ , written in terms of the spring stiffnesses [26]:

$$E = \frac{2\sqrt{3}}{h} \frac{k_n + k_s}{3k_n + k_s} k_n \quad (3a)$$

$$G = \frac{\sqrt{3}}{4h} (k_n + k_s) \quad (3b)$$

$$\nu = \frac{k_n - k_s}{3k_n + k_s} \quad (3c)$$

$$\alpha = \frac{\sqrt{3}}{2h} k_s \quad (3d)$$

$$\gamma + \varepsilon = \frac{\sqrt{3}}{h} k_\phi. \quad (3e)$$

It is evident from Eq. (3c) that the macroscopic Poisson's ratio is determined by the ratio between the shear

and normal spring stiffnesses, while the rotational spring stiffness has no influence. Negative Poisson's ratio is obtained when the shear stiffness,  $k_s$  is greater than the normal one,  $k_n$ , as also observed in other structures [41].

The constitutive Eqs. (3) formulated for the assembly of rigid units can also be used to approximate the macroscopic behaviour of the assembly of deformable units. In this case, the connection stiffnesses become a structural property of the units and the structures between them. This structural performance of the microstructural units can be purportedly designed to obtain the desired negative Poisson's ratio.

It was shown in Ref. [26] that the above description yields very accurate results when the connectors work independently, i.e. the stiffnesses at each contact point is independent of the deformation process at other contact points. In order to achieve this independence, Ref. [26] proposed to make the connections using circular arches. These arch springs are attached to a core, which is considerably stiffer than the arches. The main idea behind this concept is that the arch springs provide the flexibility in the normal direction, while the rigid core augments the shear stiffness of the unit. Figure 1a illustrates the proposed reinforced-core unit consisting of the hexagonal core and a flexible spring frame. This unit has the hexagonal symmetry required to ensure isotropy of the whole assembly, Fig. 1b. Note that instead of the solid hexagonal core other shapes may be used or it may only be partially solid as long as the core is considerably stiffer than the frame and the hexagonal symmetry is preserved.

A number of different shapes of the flexible frames and end connections were also studied in Ref. [26]. It was demonstrated that the rigid attachment of the arch spring to the core ensures that the springs work independently. It was also shown that the lower the curvature of the arch springs the higher the shear to normal stiffness ratio and consequently the stronger the auxetic effect.

This study concentrates on the ring-hexagon units shown in Fig. 1a that provide topological regularity to the assembly.

## 2.2 Reinforced rings with hexagonal core In

order to evaluate the auxetic performance of the assemblies made of the reinforced rings, we compare the stiffnesses of the arch springs in the normal and tangential directions. Figure 2 illustrates the structural model used for evaluation of the stiffnesses, which are defined as

$$k_n = \frac{P_V}{U_{VA}} \quad (4a)$$

$$k_s = \frac{P_H}{U_{HA}} \quad (4b)$$

where  $U_{VA}$  and  $U_{HA}$  are the normal and tangential displacements at the apex of the arch due to applied forces: normal  $P_V$  and tangential  $P_H$ , respectively (Fig. 2).

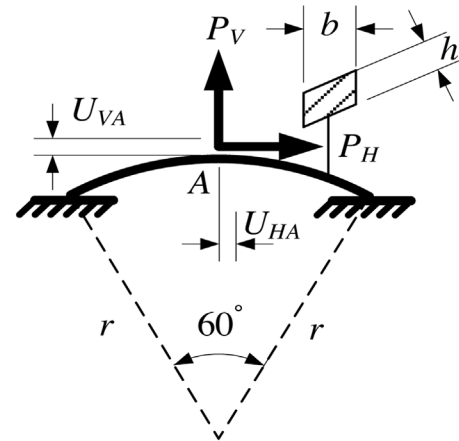


**Figure 2** Forces acting on the arch-spring and the cross-section needed for the evaluation of the normal and shear stiffnesses of the arch-spring.

To solve this problem we employ the stiffness method. We derive an analytical formulation for stiffness matrices of the arch elements as explained in Appendix B. To model the arch spring in Fig. 2, we only need two identical arch elements of opening angle  $30^\circ$ . Considering an arch made of an isotropic elastic material and a rectangular cross-section  $b \times h$  (Fig. 2), we obtain the ratio between the stiffnesses (4a and 4b) as

$$\begin{aligned} \frac{k_s}{k_n} = & \left[ (31.14 + 30.71\nu_0 + 5.1\beta^2) \right. \\ & \times (60.13 + 2.23\nu_0 - 0.7\beta^2) \times (3.8 - 3.91\nu_0 - \beta^2) \\ & \times (3648 + 3586\nu_0 + 128\nu_0^2 + 2460\beta^2 + 20\beta^4) \left. \right] / \\ & \left[ (125.4 + 17.09\nu_0 + 2.5\beta^2) \right. \\ & \times (223 - 240\nu_0 - 9\nu_0^2 + 1000\beta^2 - 6400\beta^4 + 70\nu_0\beta^2) \\ & \times (595.8 + 609.8\nu_0 + 21.8\nu_0^2 + 390\beta^2 - 80\beta^4 + 20\nu_0\beta^2) \left. \right] \quad (5) \end{aligned}$$

where  $\beta = r/h$  and  $\nu_0$  is the Poisson's ratio of the arch material. Substituting this stiffness ratio in Eq. (3c) yields the Poisson's ratio of the assembly. For instance, Fig. 3 presents the variation of Poisson's ratio as a function of  $\beta$  for a particular value of  $\nu_0 = 0.3$ . It is seen that this variation exhibits apparent minima at  $\beta = 15.169$  that corresponds to the Poisson's ratio of  $-0.66$ . These parameters are used in the following sections for the experimental and numerical investigations.

**2.3 Prototype representative cells** In order to experimentally investigate the behaviour of the core-reinforced assemblies, a number of prototypes were manufactured. The prototypes consist of a representative cell of seven core-reinforced units as shown in Fig. 4. The ratio between the radius of the unit to the thickness of the arch spring is  $\beta = 19.5$ , which, according to the

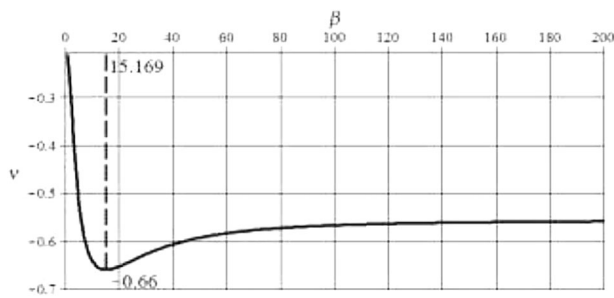


**Figure 3** Variation of the macroscopic Poisson's ratio of the reinforced-core hexagonal assembly with various ratios between the thickness of the arch-spring to unit radius,  $\beta = r/h$ .

presented theory, Eq. (5), yields the Poisson's ratio of  $-0.65$  in an infinite assembly. The out-of-plane width of the assembly is 10 mm. The links between the units are fully attached to the arch springs, Fig. 4c. The planar dimensions of the links ( $1\text{ mm} \times 1\text{ mm}$ ) make the links considerably stiffer than the arches. To maintain the rigid connection between the core and arch spring, the built-in end of the arch is made twice longer than the arch thickness, Fig. 4d (see also discussion in Section 2.1).

The prototype was design to permit application of the vertical compressive and tensile loads with special platforms for connection of the loading device. The test procedures and experimental setup are discussed in details in Section 3.

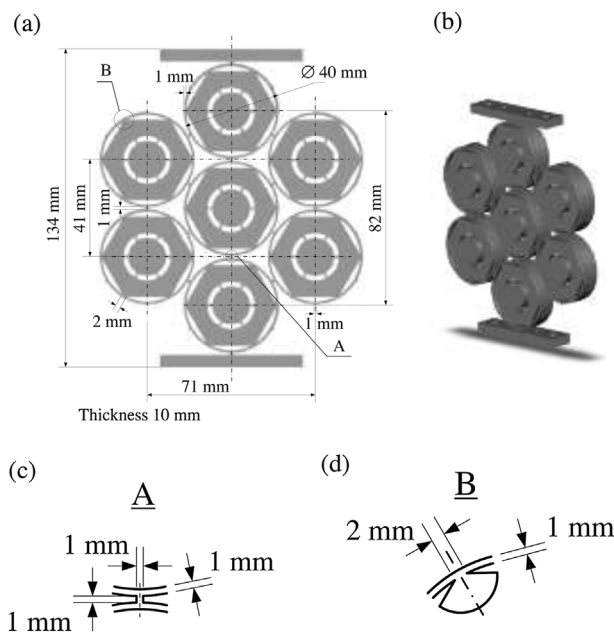


**Figure 4** 2D prototype of the reinforced-core hexagonal auxetic assembly. (a) Geometry and dimensions, (b) isometric view, (c) details of the link between the units, and (d) details of arch spring-core junction.

**Table 1** Mechanical properties of the materials used for rapid prototyping manufacturing of the prototypes.

property	units	PA2200- EOSINT-P	WaterShed 11120
density	$\text{g cm}^{-1}$	$\sim 0.44$	$\sim 1.12$
tensile modulus	MPa	1700	2765
flexural modulus	MPa	1240	2205
tensile strength	MPa	45	50
elongation at yield	%	$\sim 5$	$\sim 3.5$
elongation at break	%	20	15

Two methods were used for the fabrication of these prototypes, namely the selective laser sintering (SLS) and the stereolithography (SL). The SLS prototypes were made from fine polyamide PA2200 EOSINT P that provides high end finish along with practical functionality. The stereolithography used a water-resistant resin WaterShed 11120, which is a low viscosity liquid photopolymer producing strong parts with properties similar to ABS plastics. The mechanical properties of both prototyping materials are listed in Table 1.

### 2.4 Structural frame analysis of the prototype cells

We employ two computational methods to simulate the behaviour of the prototypes subjected to compressive and tensile load in its plane, namely the structural frame analysis based on the stiffness method and the finite element analysis. The structural model used for the frame analysis is shown in Fig. 5a. This model idealises the prototype as a plane frame with a flexible arch for the arch-springs and rigid straight members representing the reinforcement core. This frame has two planes of symmetry and therefore the computations can be reduced to the quarter cell as shown in Fig. 5b. The symmetric boundary conditions are imposed along edges at  $x=0$  and  $y=0$  as follows:

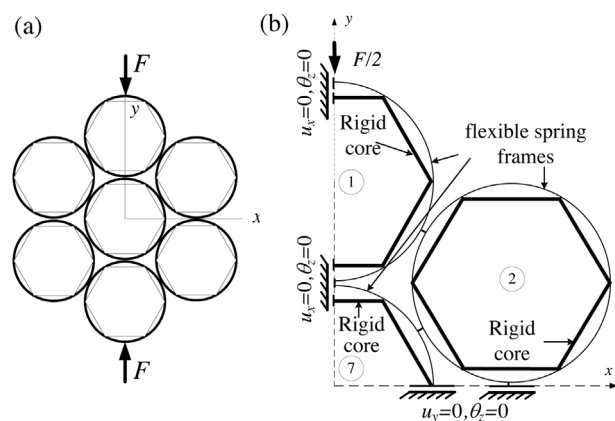


**Figure 5** Structural plane frame model of the reinforced-core hexagonal prototype. (a) Compressive test simulation, (b) computational cell utilising the symmetry of the prototype.

$$u_y(x, 0) = \theta_z(x, 0) = 0 \quad (6a)$$

$$u_x(0, y) = \theta_z(0, y) = 0 \quad (6b)$$

where  $u_x$  and  $u_y$  are the displacements in the  $x$  and  $y$  directions, respectively, and  $\theta_z$  is the rotation which represents bending.

For the solution, we use the analytical stiffness method formulated in the matrix form. The arches are modelled using the specially derived stiffness matrix (Appendix B). The rigid core and the rigid links between the units are modelled as plane frame members [93] with cross-sections much larger than the arches' profile.

### 2.5 3D finite element model of the prototype cells

An alternative method for the analysis used is the 3D finite element method. Figure 6a shows the computational model implemented using ABAQUS. We model the prototype cell using 8 node linear brick elements (C3D8R). The following meshing settings were selected through a convergence study presented in the Supporting Information. The arch was discretised with six elements through the thickness and 20 elements along the length (Fig. 6b). The links between the units were meshed with 64 elements in a square  $6 \times 6$  grid. A  $6 \times 6$  mesh was used to model the arch-core junction over the arch. The core was meshed with an  $84 \times 4$  variable grid with finer meshes next to the arch-core junctions and 4 elements were taken through the out-of-plane width of the whole assembly (Fig. 6b). In order to match the FE model with the experimental procedure, a reference point was created at the centre of each core-reinforced unit, see Fig. 6a. This point was tied to the hole in the core using the rigid body constraint implemented in ABAQUS. This modelling technique allowed for the evaluation of the unit displacements through the single reference point.

The boundary and loading conditions were defined as follows. The core of the central unit was kept immovable by prescribing zero displacements at its reference point, RP7.

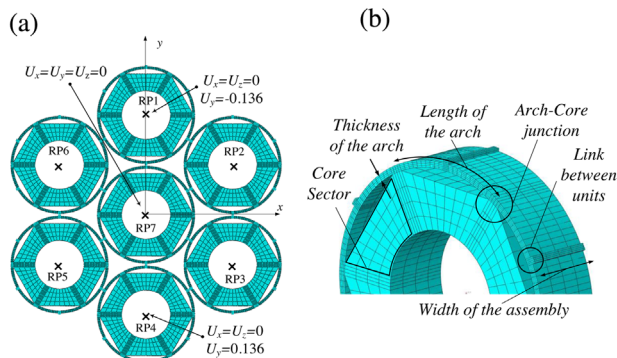


**Figure 6** 3D finite element model for the reinforced-core hexagonal prototype. (a) Geometry, loading and boundary conditions, (b) mesh settings for the single core-reinforced unit.

To ensure the planarity of the deformations the out-of-plane displacements,  $U_z$  at all reference points were restrained. The top and bottom units were pressed towards each other by uniformly distributed loads applied at the unit connectors (Fig 6a). In the numerical study presented in Section 4, a 5 MPa pressure was applied over the  $10 \text{ mm}^2$  area of the connector to produce a resultant force of 50 N.

This computational model allowed for the direct comparisons of the results with both structural frame analysis and experimental measurements.

### 3 Experimental investigation of the auxetic microstructure

A number of compression and tension tests with the prototype cells were carried out using uniaxial loading machine Instron 4301 with a calibrated loading cell of 500 N shown in Fig. 7b. The test procedure included loading and unloading sequences under displacement control mode with the bottom plate being fixed and the top plate moving with a constant velocity of  $0.1 \text{ mm min}^{-1}$  (Fig. 7b). To guarantee the conditions of small strain the displacement of the top plate was limited to 2 mm. To ensure the accurate alignment of the assembly with the loading machine, the prototype was attached to the rigid frame as

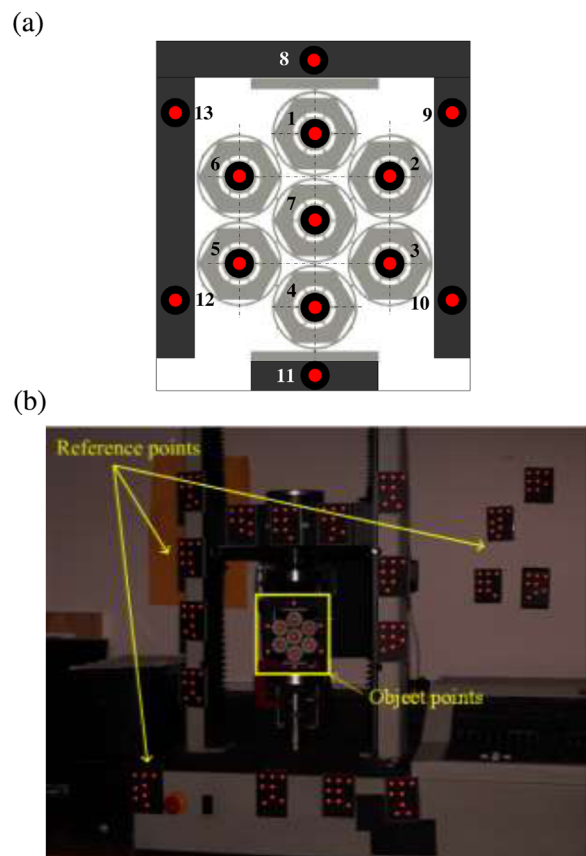


**Figure 7** Experimental setup for the photogrammetric analysis of the auxetic prototypes. (a) Mark out of the points of interest, (b) loading machine and calibration coded targets.

shown in Fig. 7. This frame was clamped to the top moveable plate, while the foot base was clamped to the bottom fixed plate. The whole frame-foot-prototype assembly was aligned into the same plane to ensure the planar nature of the deformations.

The displacements of the prototype were continuously monitored using a specially developed photogrammetric procedure for evaluation of planar deformations. In this procedure, the coordinates of the points of interest are calculated from a series of consecutively taken photographic images. To enhance the accuracy of measurements, special retro-reflective markers were used to mark the object points (Fig. 7a). The main distinctive feature of this procedure is that it allows for a simultaneous high-accuracy measurement of displacements at multiple points without interrupting the loading sequence. The details of this procedure are presented in the following subsection.

**3.1 Photogrammetric analysis of planar deformations** Photogrammetry interprets 2D measurements obtained from a set of images of an object into the network of 2D or, in the case of stereophotogrammetry, 3D coordinates defining the location and shape of that object. Photogrammetry is classified in a number of ways: (i) by the distance between the object and camera (aerial, terrestrial, close-range, macro etc.); (ii) by a number of images used for the coordinate measurements; (iii) by the method of recording; (iv) by availability of results (real-time, on-line or off-line measurements) and (v) by the application area [94]. Here we adopt an off-line close-range photogrammetry system utilizing a single high-resolution digital SLR camera and special object targets. The close range for this matter is characterised by a ratio of the camera focal length to a distance to the object between 1:20 and 1:1000. Advances in the digital photography, image processing capabilities and coded target technology made it possible to achieve measurement precision of 1:500,000 with respect to the largest object dimension in off-line photogrammetry systems [95–97] and around 1:10,000 in on-line systems [97]. In addition to the high accuracy, the close-range photogrammetry offers possibility of non-contact measurement, ability to monitor a wide network of points without any additional cost and applicability in a wide range of engineering situations. Multi- and single-camera close-range photogrammetry systems were applied to measurement of static [98–101] and dynamic deflections [102] of various civil engineering structures, capturing vibration [103] and buckling [104] modes, assessment of thermal deformations [105] and automatic crack monitoring [106, 107].

The close-range photogrammetry reconstructs the object simultaneously from several images taken from different viewpoints by creating bundles of intersecting rays and triangulation. The accuracy of photogrammetric measurements is a function of (i) the number of images (the more images used the higher the accuracy of the bundle adjustment); (ii) the spatial geometry of intersecting rays

(the wider the geometry the smaller the triangulation errors); (iii) the imaging scale (the greater the magnification the higher the accuracy of image measurements) and (iv) the camera geometric reliability and resolution (the use of so-called metric cameras with stable internal architecture and high resolutions leads to a higher precision) [94, 96]. To obtain high accuracy measurements of a stationary object, one needs to increase the number of camera views significantly by either using multiple cameras or moving the same camera around and taking many images. The latter approach, however, cannot be used to track the continuous deformation process, as an instant deformation state has to be simultaneously captured from numerous camera positions. On the other hand, the use of the multiple metric or semi-metric cameras could be restricted by the cost considerations, synchronisation problems or spatial geometry conditions. The procedure developed in this study overcomes these obstacles.

Here we develop an approach to the measurement of planar deformations under continuous loading using a single DSLR camera and the commercial photogrammetric software iWitnessPRO [108, 109]. This approach extends the standard photogrammetry technique by the following procedure. Still images of a deforming object are continuously captured during loading by the single digital camera from a fixed position. After the testing is finished, the camera is moved around and multiple images are taken ensuring wide spatial geometry. This multi-image network that also includes the fixed camera station is used to calibrate the camera and calculate the fixed camera orientation. These calibration and orientation parameters are used to evaluate the 2D deformation field based on the images taken from the fixed position. Image scanning, calculation of image coordinates, camera calibration and the multi-image bundle adjustment are accomplished using iWitnessPRO, the close-range photogrammetry software providing fully automatic 3D measurements by making use of the coded target technology. This approach does not require pre-defined information on the camera interior orientation or on the object geometry. A digital camera with a full frame sensor and a defined internal coordinate system obtained from the digital image sensor is sufficient to obtain practical accuracy measurements.

**3.2 Photogrammetric measurements of planar deformations using a single camera** Capturing deformations under continuous loading path is complicated by the fact that a large number of images required at every loading instant to achieve high accuracy measurements of 3D object coordinates. It is, however, possible to reconstruct a plane object surface from a single image provided that some information about the object geometry and interior camera orientation are known [94]. The main idea behind the proposed approach is to develop the transformation from a single image into the 2D object coordinate system using the camera information only, which can be obtained afterwards from a standard multi-image procedure. In essence, we

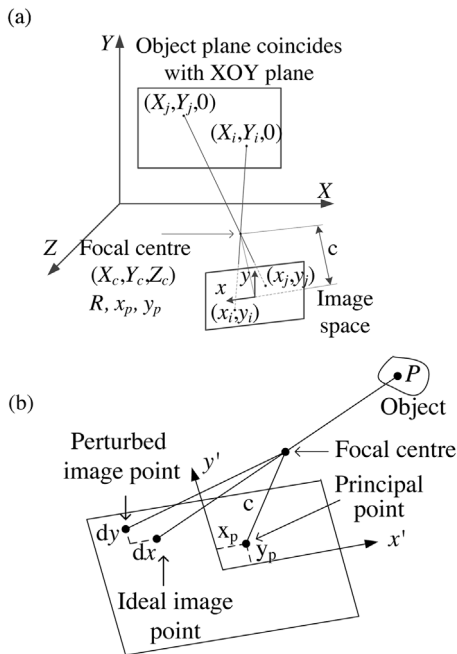


**Figure 8** The photogrammetric analysis. (a) Coordinate systems and the collinearity conditions, (b) interior orientation and camera calibration parameters.

extend the standard multi-image close-range photogrammetry technique by dividing it into two separate stages in which the unknown parameters for the reconstruction of the object displacements in the single camera stage are obtained independently from the high accuracy multi-image bundle adjustment in the second stage.

We start from a single image of the planar object. We consider two coordinate systems: the global object space coordinates  $(X, Y, Z)$  and the image space coordinates  $(x, y)$  as shown in Fig. 8a. The object system is chosen such that the  $XOY$  plane coincides with the object plane yielding  $Z = 0$  for all points located on the front face. A camera can be viewed as a spatial system consisting of a planar digital

image coordinate system to the focal centre as shown in Fig. 8a. This moves the perspective centre into the negative position and yields the vector of image coordinates defined with respect to principle point as follows [94]:

$$\mathbf{x} = \begin{Bmatrix} x - x_p \\ y - y_p \\ -c \end{Bmatrix}. \quad (7)$$

The collinearity of light rays implies that the object point, image point and perspective centre all lie along a straight line. Thus, the central perspective transformation applies at each point as [94]

$$\begin{Bmatrix} x_i - x_p \\ y_i - y_p \\ -c \end{Bmatrix} = \lambda \mathbf{R} \begin{Bmatrix} X_i - X_c \\ Y_i - Y_c \\ Z_i - Z_c \end{Bmatrix} \quad (8)$$

where  $\mathbf{R}$  is the orthogonal rotational matrix describing the relative orientation between the global object space coordinates  $(X_i, Y_i, Z_i)$  and the image space coordinates  $(x_i, y_i)$ ,  $\lambda$  is the scale factor,  $X_c, Y_c,$  and  $Z_c$  are the coordinates of the camera position taken at the origin of the image coordinate system (the camera focal centre).

The complete spatial rotation of the camera image system is defined by successive application of three individual rotations about the global coordinate axes as follows. The first rotation, the azimuth,  $\alpha$ , is a right hand rotation about the  $Z$ -axis, the second, elevation,  $\varepsilon$ , is a right hand one about the first rotated  $X$ -axis, and the third, roll,  $\kappa$  is a left hand rotation about the twice rotated  $Y$ -axis. As a result, we have

$$\mathbf{R} = \mathbf{R}_\kappa \mathbf{R}_\varepsilon \mathbf{R}_\alpha \quad (9)$$

where  $\mathbf{R}_\kappa, \mathbf{R}_\varepsilon$  and  $\mathbf{R}_\alpha$  are the 2D rotation matrices defined by the direction cosines of the axes rotated as described above. This leads to

$$\mathbf{R} = \begin{bmatrix} \cos(\alpha)\cos(\kappa) + \sin(\alpha)\sin(\varepsilon)\sin(\kappa) & \sin(\alpha)\cos(\kappa) - \cos(\alpha)\sin(\varepsilon)\sin(\kappa) & \cos(\varepsilon)\sin(\kappa) \\ -\cos(\alpha)\sin(\kappa) + \sin(\alpha)\sin(\varepsilon)\cos(\kappa) & -\sin(\alpha)\sin(\kappa) - \cos(\alpha)\sin(\varepsilon)\cos(\kappa) & \cos(\varepsilon)\cos(\kappa) \\ \sin(\alpha)\cos(\varepsilon) & -\cos(\alpha)\cos(\varepsilon) & -\sin(\varepsilon) \end{bmatrix}. \quad (10)$$

sensor and the lens with a focal centre at a fixed distance (focal length) from the image plane as shown in Fig. 8b. The coordinate system  $(x', y')$  defined by the pixel array is centred on the image. The camera interior orientation (IO) describes the spatial position of the focal centre through the principal point offsets  $(x_p, y_p)$  and the principle distance  $c$  (Fig. 8b). The principal distance is the lens focal length with the addition of an extension required to achieve sharp focus. It is common in the photogrammetry literature to shift the

The rotations  $(\alpha, \varepsilon$  and  $\kappa)$  and the coordinates of camera position  $(X_c, Y_c$  and  $Z_c)$  all together define the exterior orientation (EO) of the camera station.

Inverting Eq. (8) we obtain the object coordinates as

$$\begin{Bmatrix} X_i \\ Y_i \\ Z_i \end{Bmatrix} = \lambda^{-1} \mathbf{R}^T \begin{Bmatrix} x_i - x_p \\ y_i - y_p \\ -c \end{Bmatrix} + \begin{Bmatrix} X_c \\ Y_c \\ Z_c \end{Bmatrix}. \quad (11)$$

To eliminate the scale factor,  $\lambda$ , we divide the first two Eq. (11) by the third one and after substituting  $Z_i = 0$  obtain

$$X_i = X_c - Z_c \frac{R_{11}(x_i - x_p) + R_{21}(y_i - y_p) - R_{31}c}{R_{13}(x_i - x_p) + R_{23}(y_i - y_p) - R_{33}c} \quad (12a)$$

$$Y_i = Y_c - Z_c \frac{R_{12}(x_i - x_p) + R_{22}(y_i - y_p) - R_{32}c}{R_{13}(x_i - x_p) + R_{23}(y_i - y_p) - R_{33}c}. \quad (12b)$$

It is seen that in order to calculate the unknown object coordinates ( $X_i, Y_i$ ) we need to know the camera interior and exterior orientations. To obtain it, we use another series of images, which is called a calibration bundle. This calibration bundle is shot independently and may include the large number of camera stations with wide spatial geometry. We add to this bundle the fixed camera station and apply the multi-image photogrammetric restitution allowing for the camera self-calibration and recovery of the exterior orientation for all camera stations. Finally, we substitute the fixed camera orientation obtained from this calibration into Eqs. (12) and calculate the object coordinates for all points that lie on the front face of the object. Using the images taken from this single camera during loading, we determine the displacements at multiple points corresponding to each image. It is important to note that if the camera position firmly fixed during the loading, we need only one calibration bundle shot at the end of the loading procedure. The number of images taken during loading is only limited by the speed of the camera.

**3.3 Camera self-calibration** In photogrammetry, the calibration process includes determination of interior orientation and image distortion parameters due to departure from collinearity. This is commonly done through a self-calibrating bundle adjustment in a multi-station network of images [97, 108, 110, 111]. The departures from collinearity in the close-range photogrammetry occur as a result of: (i) lens distortion; (ii) errors in interior orientation and (iii) focal plane unflatness. The deviation from a straight line leads to a perturbation in the image point location ( $dx, dy$ ) as shown in Fig. 8b. Consequently, the following correction terms should be subtracted from the image coordinates:

$$dx = dx_{\text{radial}} + dx_{\text{decenter}} + dx_{\text{IO}} + dx_{\text{unflat}} \quad (13a)$$

$$dy = dy_{\text{radial}} + dy_{\text{decenter}} + dy_{\text{IO}} + dy_{\text{unflat}}. \quad (13b)$$

The lens distortion has two components: the symmetric radial ( $dx_{\text{radial}}, dy_{\text{radial}}$ ) and decentring ( $dx_{\text{decenter}}, dy_{\text{decenter}}$ ) distortions defined as follows [94]:

$$dx_{\text{radial}} = \frac{x}{r_i} \Delta r_i, \quad dy_{\text{radial}} = \frac{y}{r_i} \Delta r_i \quad (14)$$

with  $r_i = \sqrt{(x_i - x_p)^2 + (y_i - y_p)^2}$  and  $\Delta r_i = K_1 r_i^3 + K_2 r_i^5 + K_3 r_i^7$ ;

$$dx_{\text{decenter}} = P_1(3x_i^2 + y_i^2) + 2P_2 x_i y_i \quad (15a)$$

$$dy_{\text{decenter}} = 2P_1 x_i y_i + P_2(x_i^2 + 3y_i^2) \quad (15b)$$

where  $K_1, K_2, K_3, P_1$  and  $P_2$  are the coefficients determined during the self-calibration process.

In general, the perturbation due to the radial distortion is most significant; even for the metric (high precision cameras)  $\Delta r_i$  can be substantial. The radial distortion changes with focusing and zoom and it is usually 10 times more significant than the decentring distortion. The decentring distortion arises from ill-centred lens components and causes tangential and radial image shifts [94].

Errors in the interior orientation ( $x_p, y_p, c$ ) are also directly rectified during the self-calibration bundle adjustment. The effect of the focal plane unflatness in digital arrays is usually ignored, mostly due to a lack of a practical way to determine it.

Nowadays, the self-calibration bundle adjustment is a well-developed procedure incorporated in all photogrammetry packages. In iWitnessPRO, the camera calibration is performed automatically with the aid of coded targets [109].

**3.4 Targeting and illumination** To achieve highly accurate measuring results, the points of interest on the object are marked using special retro-reflective targets shown in Fig. 9 (see also Fig. 7). The retro-reflectors return light very efficiently to the light source. Thus, when such target is illuminated by a flash located at the camera, the target exposure is in sharp contrast with the object background, which enhances their automatic detection. These points can be easily detected and measured to a precision in image space of 0.03–0.05 pixels [94, 108].

Figure 9 also shows the coded retro-reflective targets used as the reference points by iWitnessPRO. These targets are a special type of target that the software can recognise and use for automatic scaling and self-calibration.

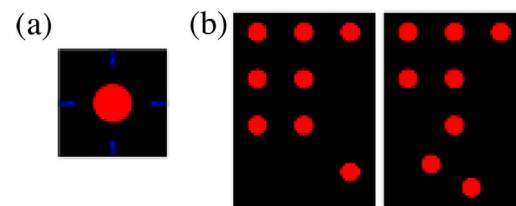


**Figure 9** Retro-reflective targets. (a) Single retro-reflective target to mark points of interest, (b) coded targets used for automatic scaling and self-calibration.

**3.5 Measurement procedure** The procedure presented in Sections 3.2–3.4 was integrated into the experimental setup for the testing of the 2D auxetic prototypes described in Section 2.3. We use the single retro-reflective targets to mark 7 points on the face of the prototype on the reinforcing core of each unit, another 5 on the rigid frame and a single point on the bottom base as shown in Fig. 7a. The coded targets were distributed around the prototype to provide the wide spatial geometry for the calibration bundle (Fig. 7b).

For the measurements, we used Canon 5D Mark II DSLR full frame camera with resolution of  $5616 \times 3744$  pixels, CCD format of  $35 \times 24$  mm, pixel size of 0.0064 mm, and a SIGMA lens with fixed focal length of 70 mm. In order to synchronise the loading device records with the photogrammetric measurements, the camera was connected to the PC attached to the setup. This also allowed for the remote control of the camera and the direct downloading of the images. The camera was mounted on a rigid stand in front of the loading machine to secure the fixed camera orientation.

The following measurement sequence was implemented. Photographs of the object during loading sequence were taken from the fixed camera position with constant intervals of 6 s. At the end of the testing, the prototype was unloaded and the calibration series were shot. The calibration bundle consisted of 70 stations widely scattered around the object and loading machine. At each camera station, four images were taken to exam the repeatability of the measurements. These calibration bundles were processed by iWitnessPRO through the automatic image measurement and the multi-image bundle adjustment that resulted in the determination of interior and exterior orientations and the calibration parameters for all camera stations including the main fixed position. To obtain the image coordinates of the 13 object points of interest, the loading sequence images were processed using the iWitness's image measurement feature. These image coordinates were adjusted using the image distortion coefficients obtained from the self-calibration and used to calculate the object coordinates at every time point.

**4 Results and discussions** In this section, we present the results of the experimental procedures outlined above. We show the typical results obtained over a large number of experiments. We demonstrate the realisable accuracy of the photogrammetric procedure developed and discuss the evaluation of the Poisson's ratios.

In order to define the 2D deformations, we use the distances between the object points shown in Fig. 7a. These distances vary during loading, which can be used to calculate the strain. In order to compare the results, we apply similar approach to the numerical simulations as well.

The verification of the photogrammetric measurement procedure is presented in Appendix C. It is demonstrated that the high accuracy measurement is achieved with average relative errors of 0.019%.

**4.1 Poisson's ratio in the reinforced core auxetic assemblies** We define the effective Poisson's ratio of the prototype based on the displacements of the reinforced units as the lateral to axial strain ratio. The axial strain is given in the loading (vertical) direction by the extension/contraction of the distance 1\_4, while the lateral strain is represented by the horizontal distances 2\_6 and 3\_5 (Fig. 7a). Thus the macroscopic Poisson's ratio can be determined as

$$\nu_{\text{eff}} = -\frac{\varepsilon_H}{\varepsilon_V} = -\frac{\langle \Delta d_{2_6}, \Delta d_{3_5} \rangle}{\langle d_{2_6}, d_{3_5} \rangle} \bigg/ \frac{\Delta d_{1_4}}{d_{1_4}} \quad (16)$$

where  $d_{i_j}$  is the distance between the points  $i$  and  $j$  on the undeformed body,  $\Delta d_{i_j}$  is the corresponding extension and  $\langle \rangle$  denotes volumetric (surface) averaging. This description eliminates the influence of the local deformations that occur at the top and bottom arch springs connected to the loading device and allows for capturing the interaction between the structural units.

The extensions are calculated through the linear regression analysis of the load-extension data obtained by synchronisation of the records from the load cell and the photogrammetric measurements. Figure 10 demonstrates the typical results for the compression test sequences. The experimental data are presented together with the corresponding linear regression equations and the coefficients of determination,  $R^2$ . It is seen that the data fit very well into the linear model for both vertical and horizontal distances. The results for the distance 8\_11 also correlate very well with the crosshead displacements. The prototype is exhibiting the auxetic behaviour by simultaneously contracting in both directions. Similar behaviour is also observed in the tension test sequence shown in Fig. 11: the gradients of the trend lines for the extension 8\_11 and the crosshead displacement coincide as well as the gradients of the trend lines for distances 2\_6 and 3\_5. We use these displacement gradients in the subsequent calculations of the vertical and horizontal strains and the effective Poisson's ratio as follows:

$$\varepsilon_V = \frac{F}{S_{1_4} d_{1_4}} \quad (17a)$$

$$\varepsilon_H = \left\langle \frac{F}{S_{2_6} d_{2_6}}, \frac{F}{S_{3_5} d_{3_5}} \right\rangle \quad (17b)$$

where  $F$  is the applied load and  $S_{i_j}$  are the slopes of the trend lines obtained through the linear regression analysis.

We apply the same approach to the numerical assessment of the effective Poisson's ratio. Table 2 presents the results obtained using two computational models described in Sections 2.4 and 2.5. For these calculations, we use the material properties of the SLS prototypes (Table 1). The strain is calculated based on the displacements of the rigid cores of the units. It is seen that in terms of

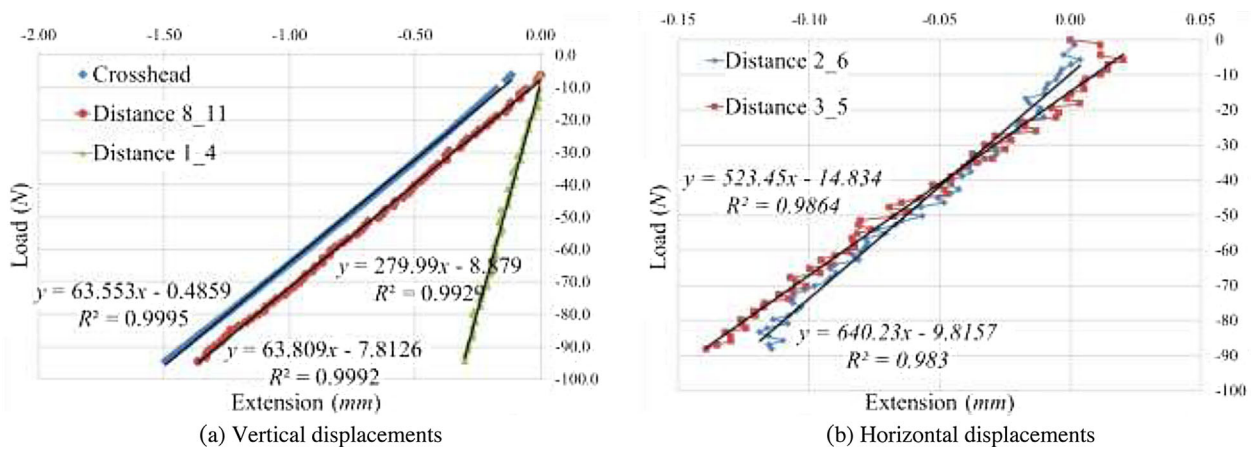


**Figure 10** Compression test sequence. (a) Vertical displacements and the change of vertical distances between points 8 and 11 (8\_11) and 1 and 4 (1\_4), Fig. 7; (b) horizontal displacements and the change of horizontal distances between points 2 and 6 (2\_6) and 3 and 5 (3\_5), Fig. 7. The data points represent the measurements; the straight lines represent the corresponding linear regressions indicated by the equations shown at the lines.

the effective Poisson's ratio both models come to a good agreement.

Figure 12 shows all results obtained for the effective Poisson's ratio in the reinforced core assemblies. It is seen that six tests consisting of the tensile and compressive loading and unloading sequences provide very close results with the average Poisson's ratio of  $-0.589$  and the relative standard deviation of  $9.22\%$ . These values also agree with the computational simulations yielding the differences of  $7.66\%$  to the FE method and  $19.5\%$  to the idealised frame model. Furthermore, by relating these results to the theoretical predictions made for an infinite assembly (Fig. 3), we can observe that the predicted value of the Poisson's ratio of  $-0.65$  given in Section 2.3 differs from the experimentally found macroscopic Poisson's ratio by only  $9.2\%$ .

Although, the prototype cells used in this study do not completely represent the infinite regular assembly (Fig. 1), it is seen that under the available type of loading and boundary conditions the reinforced-core assemblies approximate the infinite assembly producing strong auxetic effect.

**5 Summary and conclusions** An experimental investigation was carried out to validate the predicted auxetic behaviour of the reinforced-core microstructural units. This concept directly implements the idea that in order to create a structure macroscopically exhibiting negative Poisson's ratio, the capacity of the microstructure to prevent the angle change or shear has to be higher than the resistance to volumetric deformation. In the proposed reinforced-core units, the normal stiffness is controlled by a flexible frame that forms local arch springs at the contact points.

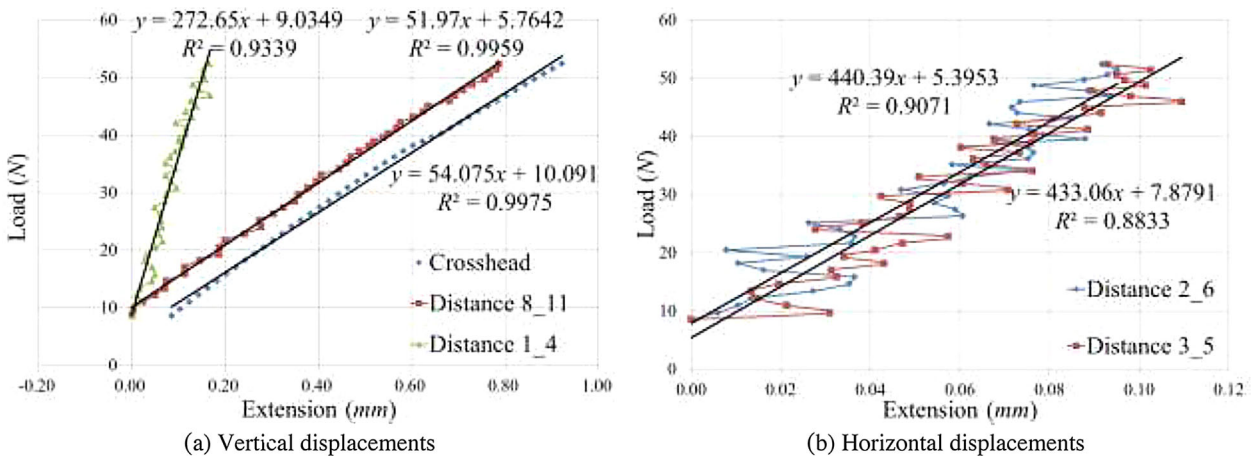


**Figure 11** Tension test sequence. (a) Vertical displacements and the change of vertical distances between points 8 and 11 (8\_11) and 1 and 4 (1\_4), Fig. 7. (b) Horizontal displacements and the change of horizontal distances between points 2 and 6 (2\_6) and 3 and 5 (3\_5), Fig. 7. The data points represent the measurements; the straight lines represent the corresponding linear regressions indicated by the equations shown at the lines.

**Table 2** Comparisons of the results obtained using different simulation models,  $F = 50$  N.

distances	solid model (ABAQUS)			frame model (the stiffness method)		
	original (mm)	deformed (mm)	strain (%)	original (mm)	deformed (mm)	strain (%)
7_1	41.0	40.86	-0.332	41.0	40.88	-0.293
7_2	41.0	40.94	-0.153	41.0	40.96	-0.092
7_3	41.0	40.94	-0.153	41.0	40.96	-0.092
7_4	41.0	40.86	-0.332	41.0	40.88	-0.293
7_5	41.0	40.94	-0.153	41.0	40.96	-0.092
7_6	41.0	40.94	-0.153	41.0	40.96	-0.092
2_6	71.0	70.88	-0.185	71.0	70.91	-0.145
3_5	71.0	70.88	-0.185	71.0	70.91	-0.145
1_4	82.0	81.73	-0.332	82.0	81.76	-0.293
Poisson's ratio			-0.5570			-0.4933

The tangential movement on the other hand is resisted by the rigid cores that enhance the ability of the frame to retain the global shape.

In this study, we considered hexagonal packing of the reinforced-core units, which ensures isotropy in its plane. The theoretical estimates of the macroscopic (effective) moduli for these structures were made using the Cosserat continuum model, which was originally developed for a planar assembly of rigid particles and adapted here for the modelling of flexible units.

Based on this theoretical development, a number of physical prototypes were designed and subsequently manufactured by stereolithography and selective laser sintering rapid prototyping techniques. The prototypes were made as planar hexagonal cells comprising of seven reinforced-core units. A series of uniaxial loading tests was carried out to evaluate the macroscopic Poisson's ratios of these assemblies.

In order to simultaneously monitor the deformations at any number of points developed in the prototype structures under loading, we employed the close-range photogrammetry method. We developed the procedure to measure the planar deformations using a single digital camera. We

showed that the deformation field can be measured continuously without interrupting the loading sequence and the acquisition rate (a number of images) is only limited by the speed of the camera. The high accuracy was achieved even by using a consumer grade digital camera. The camera was self-calibrated during the image processing.

The test results showed that these isotropic assemblies are able to produce strong auxetic behaviour with the Poisson's ratio as low as  $-0.6$ . The results agree very well with the direct numerical analysis of the prototypes and validate the theoretical predictions. This study compliments the development of the design concept for creating planar auxetic structures with the reinforced-core units.

**Supporting Information** Additional supporting information may be found in the online version of this article at the publisher's web-site.

**Acknowledgements** The authors acknowledge the financial support from the Australian Research Council initially through the Discovery Grant DP0773839 and then through the ARC Linkage Project Grant LP120100299 with the sponsorship of AWE Ltd and Norwest Energy.

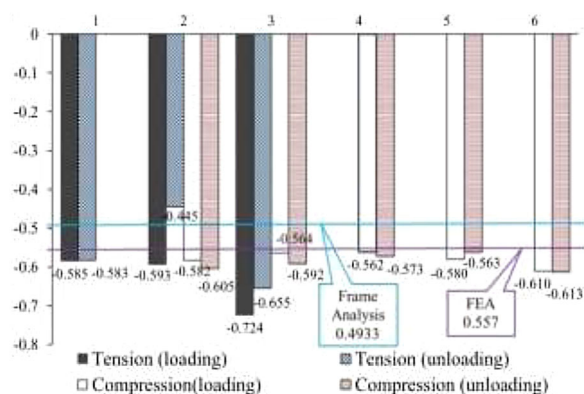


**Figure 12** The effective (macroscopic) Poisson's ratio in the reinforced core auxetic assemblies: experimental and theoretical evaluation.

## Appendix A Homogenisation by differential expansions of regular assemblies of rigid particles – Cosserat continuum

We consider a periodic assembly of rigid spherical particles elastically bonded to each other. We assume that connections between the spheres are symmetrically distributed, such that each connection has a symmetric counterpart on the other side of a sphere. Each connection is described using six linear springs: one normal and two tangential (shear) translation springs of stiffness  $k_1$ ,  $k_2$  and  $k_3$ , respectively, and three rotational springs of stiffness  $k_{\phi 1}$ ,  $k_{\phi 2}$  and  $k_{\phi 3}$  [26, 48]. In order to develop a continuum model for a general sphere assembly, we start from a two-sphere interaction and then generalise it for the specific arrangements. We use two coordinate systems: a local one ( $X_1$ ,  $X_2$ ,  $X_3$ ) located at the centre of the reference sphere with the  $X_1$

axis aiming at the centre of the connected sphere (Fig. A1a) and a global system  $(x_1, x_2, x_3)$  defining the general axes of the assembly and obtained by rotation of the local axes (Fig. A1b).

The potential discrete energy density of the two-sphere interaction is defined in terms of spring stiffnesses oriented in the directions of the local coordinate axes as

$$W_0 = \frac{1}{2}k_j(\Delta u'_j - r\varepsilon_{1jk}\Sigma\phi'_k)^2 + \frac{1}{2}k_{\phi,j}\Delta\phi_j'^2, \quad (A.1)$$

$i, j, k = 1 \dots 3$

where  $\Delta u'_j$  and  $\Delta\phi'_j$  is the relative discrete translations and rotations between two spheres in the directions of the local axes,  $r$  is the radius of a sphere,  $\Sigma\phi'_k$  is the summation of corresponding discrete rotations of two spheres, and  $\varepsilon_{ijk}$  is Levi-Civita symbol (Fig. A1a). The transformation from the local coordinates into the global ones yields

$$W_0 = \frac{1}{2}k_j(R_{ji}\Delta u_i - r\varepsilon_{1jl}R_{li}\Sigma\phi_i)^2 + \frac{1}{2}k_{\phi,j}(R_{ji}\Delta\phi_i)^2, \quad (A.2)$$

$i, j, l = 1 \dots 3$

where  $R_{ji}$  are the terms of the rotational matrix given as

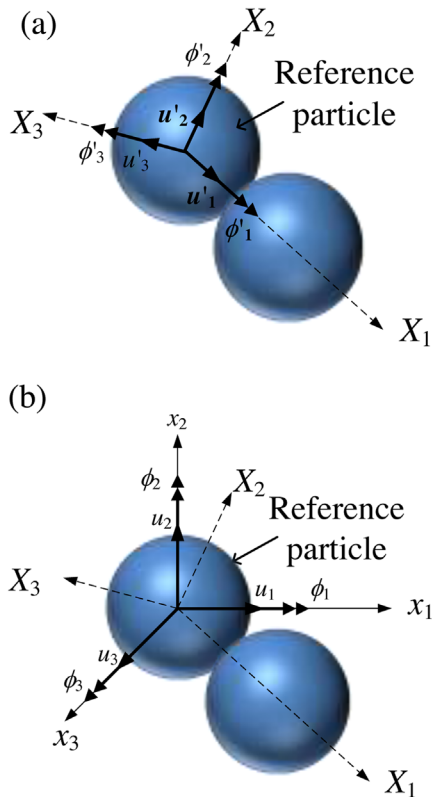


**Figure A1** Geometry and coordinate systems for the two-sphere interaction. (a) Local coordinates and displacements, (b) global coordinates and displacements.

$$\mathbf{R} = \begin{bmatrix} \cos(\psi)\cos(\theta) & \cos(\psi)\sin(\theta) & -\sin(\psi) \\ -\sin(\theta) & \cos(\theta) & 0 \\ \sin(\psi)\cos(\theta) & \sin(\psi)\sin(\theta) & \cos(\psi) \end{bmatrix}. \quad (A.3)$$

This transformation is defined by two rotations  $\theta$  and  $\psi$ . The first angle,  $\theta$  is a ‘right-handed’ rotation about the  $x_3$  axis (clockwise when looking out along the axis) resulting in a planar transformation in the  $x_1$ - $x_2$  plane. The second angle,  $\psi$  is a ‘right-handed’ rotation about the first rotated  $x_2$  axis and it directs the rotated  $x_1$  axis to the centre of the contacting sphere.

Now we apply the homogenisation procedure by differential expansions [82] as follows. We replace the finite differences in Eq. (A.2) with corresponding Taylor expansions. Keeping the leading terms of the series up to the second order, we obtain

$$W(x_1, x_2, x_3) = 2r^2k_j\left(R_{ji}R_{1m}\frac{\partial u_i}{\partial x_m} - \varepsilon_{1jl}R_{li}\phi_i\right)^2 + 2r^2k_{\phi,j}\left(R_{ji}R_{1m}\frac{\partial\phi_i}{\partial x_m}\right)^2, \quad i, j, l, m = 1 \dots 3 \quad (A.4)$$

where  $u_i$  and  $\phi_i$  are the displacement and rotation functions of the global coordinates  $x_1, x_2$  and  $x_3$ . Then using the Cosserat continuum deformation measures we obtain

$$W(x_1, x_2, x_3) = 2r^2k_j(R_{ji}R_{1m}\gamma_{mi})^2 + 2r^2k_{\phi,j}(R_{ji}R_{1m}\chi_{mi})^2, \quad (A.5)$$

$i, j, m = 1 \dots 3$

with Cosserat strains  $\gamma_{mi}$  and curvatures  $\chi_{mi}$  are defined as [85]

$$\gamma_{mi} = u_{i,m} - \varepsilon_{lmi}\phi_l \quad (A.6)$$

$$\chi_{mi} = \phi_{i,m}. \quad (A.7)$$

The total energy density of a regular arrangement of rigid spheres is obtained as follows. Firstly, we define the orientation of all contact pairs at the reference particle. Secondly, we sum up the energy of these interactions using Eq. (A.5) and then divide it by the volume of the unit cell corresponding to this packing arrangement.

The constitutive relations are obtained by variation of the total homogenised energy density with respect to the corresponding deformation measures as

$$\sigma_{mi} = \frac{\partial W_{\text{total}}}{\partial \gamma_{mi}}, \quad \mu_{mi} = \frac{\partial W_{\text{total}}}{\partial \chi_{mi}} \quad (A.8)$$

where  $\sigma_{mi}$  and  $\mu_{mi}$  are the Cosserat stress and couple stress tensors respectively.

### Appendix B Derivation of the stiffness matrix for the half arch spring

Consider an arch element of radius  $r$  and an opening angle  $30^\circ$  shown in Fig. B1a. This element is characterised by six degrees of freedom in its plane (Fig. B1a). We derive the stiffness matrix from the flexibilities corresponding to these degrees of freedom [93, 112]. As the arch springs can be very short, we include the effect of the transverse shear on the deformations.

First we consider the arch element shown in Fig. B1b. The flexibility matrix is defined by the displacements caused by the corresponding unit loads. To determine the relationship we consider the strain energy of the arch element

$$U = \frac{1}{2} \int_0^{\pi/6} \left( \frac{M(\theta)^2}{EI} + k_{SCF} \frac{Q(\theta)^2}{GA} + \frac{N(\theta)^2}{EA} \right) r d\theta \quad (\text{B.1})$$

where  $M(\theta)$ ,  $Q(\theta)$  and  $N(\theta)$  are the bending moment, shear force and axial force, respectively. They are defined from equilibrium conditions and vary with the arch angle coordinate.  $G$  and  $E$  are the shear and Young's moduli,  $I$  and  $A$  are the moment of inertia and the area of the cross-section, and  $k_{SCF}$  is the shear correction factor compensating for the inconsistency between the true parabolic distribution of the shear stress and the assumed constant one [113].

The internal forces and the moment read (Fig. B1c)

$$\begin{aligned} N(\theta) &= -X_1 \cos(\theta) + X_2 \sin(\theta) \\ Q(\theta) &= -X_1 \sin(\theta) - X_2 \cos(\theta) \end{aligned} \quad (\text{B.2})$$

$$M = X_1 r(1 - \cos(\theta)) + X_2 r \sin(\theta) - X_3.$$

The flexibility coefficients at the left end of the arch element are obtained using Castigliano's second theorem [113] as

$$F_{ij}^{(L)} = \left. \frac{\partial U}{\partial X_j} \right|_{X_{i=j}=1, X_{i \neq j}=0} \quad (\text{B.3})$$

Thus the symmetric terms of the flexibility matrix read

$$F_{1,1}^{(L)} = \left( \frac{\pi}{4} - 1 + \frac{\sqrt{3}}{8} \right) \frac{R^3}{EI} + k_{SCF} \left( \frac{\pi}{12} - \frac{\sqrt{3}}{8} \right) \frac{R}{GA} + \left( \frac{\pi}{12} + \frac{\sqrt{3}}{8} \right) \frac{R}{EA},$$

$$F_{1,2}^{(L)} = \left( \frac{7}{8} - \frac{\sqrt{3}}{2} \right) \frac{R^3}{EI} + k_{SCF} \frac{R}{8GA} - \frac{R}{8EA},$$

$$F_{1,3}^{(L)} = \left( \frac{1}{2} - \frac{\pi}{6} \right) \frac{R^2}{EI},$$

$$F_{2,2}^{(L)} = \left( \frac{\pi}{12} - \frac{\sqrt{3}}{8} \right) \frac{R^3}{EI} + k_{SCF} \left( \frac{\pi}{12} + \frac{\sqrt{3}}{8} \right) \frac{R}{GA} + \left( \frac{\pi}{12} - \frac{\sqrt{3}}{8} \right) \frac{R}{EA},$$

$$F_{2,3}^{(L)} = \left( \frac{\sqrt{3}}{2} - 1 \right) \frac{R^2}{EI},$$

$$F_{3,3}^{(L)} = \frac{\pi R}{6EI}. \quad (\text{B.4})$$

By inverting the matrix (B.4) we obtain the stiffnesses at the left end of the element corresponding to the unit displacements in the directions 1 and 2 and the rotation 3 ( $S_{ij}$  with  $i = 1 \dots 3, j = 1 \dots 3$ ). The stiffnesses at the right end due to unit displacements in the degrees of freedom 1 ... 3 are found from the equilibrium considerations as follows

$$S_{4,j} = -\frac{\sqrt{3}}{2} S_{1,j} + \frac{1}{2} S_{2,j}, \quad j = 1 \dots 3$$

$$S_{5,j} = -\frac{1}{2} S_{1,j} - \frac{\sqrt{3}}{2} S_{2,j}, \quad j = 1 \dots 3$$

$$S_{6,j} = S_{1,j} r \left( 1 - \frac{\sqrt{3}}{2} \right) + \frac{1}{2} S_{2,j} r - S_{3,j}, \quad j = 1 \dots 3. \quad (\text{B.5})$$

Terms  $S_1 \dots 3, 5 \dots 6$  are found from the symmetry considerations and then terms  $S_4 \dots 6, 5 \dots 6$  are determined using Eqs. (B.5) for  $j = 5 \dots 6$ .

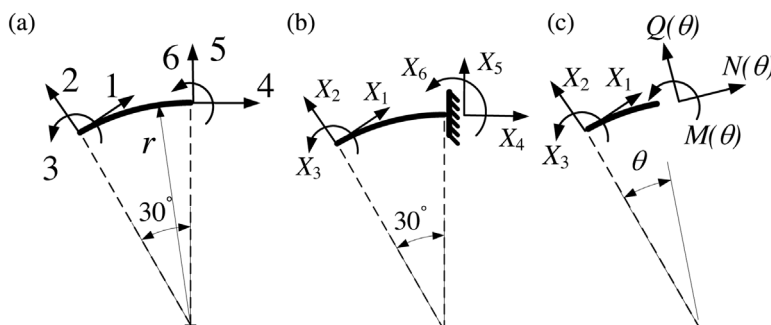


**Figure B1** Planar arch element with opening angle of  $30^\circ$ , (a) translational and rotational degrees of freedom, (b) flexibility coefficients at the left end of the arch element and (c) internal forces and moments.

**Appendix C Verification of the photogrammetric measurements**

The verification of the developed procedure is conducted in two ways. Firstly, we examine the accuracy of the bundle adjustment of the multi-shot calibration series. We compare the results obtained by processing the 4 series of images taken from the identical camera position (Section 3.4). Table C1 shows the relative deviations between these bundles presented in terms of the maximum and average relative standard deviation values for various numbers of camera stations and distance ranges. It is seen that the higher accuracy is achieved for the longer distances measured

using more camera stations. Table C2 demonstrates typical results of the camera calibration obtained from the multi-shot bundle adjustment. The results are averaged over four series and presented along with the relative deviations. We can observe that a reasonable accuracy is obtained for all measurements and that the accuracy of the angle measurements is noticeably better than that of the distance measurements.

To investigate the accuracy of the single camera measurements we use the measurements at the rigid points. These points lie on the rigid frame and do not move with respect to each other, which has to lead to zero displacement

**Table C1** Multi-shot calibration bundle: repeatability accuracy.

test	no. of stations	distance range (mm)	MAX**(STD/AVE)* (%)	AVE** (STD/AVE)* (%)
1	84	<45	0.0070	0.0048
2	84	<45	0.0079	0.0056
3	85	<45	0.0104	0.0069
3	85	60 ... 150	0.0090	0.0058
4	71	60 ... 150	0.0210	0.0103
5	71	<45	0.0283	0.0283
5	71	60 ... 150	0.0209	0.0140
6	71	60 ... 150	0.0050	0.0039
7	71	<30	0.0126	0.0098
7	71	60 ... 90	0.0055	0.0031
7	71	>130	0.0017	0.0014

\*STD/AVE is the relative standard deviations between four measurements of the same distance obtained by processing the four series of images taken from the identical camera position (Section 3.4)

\*\*MAX (STD/AVE) and AVE (STD/AVE) stand for the maximum and average of the relative deviations STD/AVE over a particular range distance, respectively.

**Table C2** Calibration bundle adjustment: exterior and interior orientations together with self-calibration for the single camera station.

EO*	$X_c$	$Y_c$	$Z_c$	azimuth, $\alpha$	elevation, $\varepsilon$	roll, $\kappa$
value	-132.10 mm	206.95 mm	2391.6 mm	-2.046 rad	-1.497 rad	2.026 rad
STD/AVE	1.156 %	0.176 %	0.317 %	0.190%	-0.030%	0.193%
IO**	$c$	$x_p$	$y_p$			
value	70.08 mm	0.129 mm	0.150 mm			
STD/AVE	0.33 %	2.33 %	1.09 %			
self-calibration***	$K_1$	$K_2$	$K_3$	$P_1$	$P_2$	
value	$-9.5 \times 10^{-6}$	$-1.1 \times 10^{-8}$	$-8.3 \times 10^{-12}$	$-8.9 \times 10^{-7}$	$-9.1 \times 10^{-6}$	
STD/AVE	-1.012%	-9.507%	-	-2.8073%	-1.488%	

\*EO is the camera exterior orientation defined by the position coordinates ( $X_c$ ,  $Y_c$  and  $Z_c$ ) and three rotations ( $\alpha$ ,  $\varepsilon$  and  $\kappa$ ), Fig. 8a.

\*\*IO is the camera interior orientation defined by the principal point offsets ( $x_p$ ,  $y_p$ ) and the principle distance  $c$ , Fig. 8b.

\*\*\*The parameters of lens distortion computed in the process of self-calibration, Eqs. (13 and 15), Section 3.2.

**Table C3** Measurements at the rigid points for the compression and tension tests.

distances*	12_13	13_8	8_9	9_10	13_9	12_10	12_9	13_10
compression test								
average (mm)	63.895	86.349	85.538	63.917	131.949	132.503	146.999	146.718
STD/AVE**, %	0.019	0.013	0.010	0.013	0.005	0.006	0.007	0.007
tension test								
average (mm)	63.891	86.352	85.544	63.910	131.955	132.510	147.015	146.711
STD/AVE**, %	0.015	0.012	0.014	0.022	0.007	0.007	0.007	0.007

\*Each pair indicates the distance between the points connected by underscore, Fig. 7.

\*\*STD/AVE is the relative standard deviations for the measurements of distances between the rigid points obtained from different images.

deviation. Table C3 presents the typical measurement obtained at the rigid points in the tension and compression tests. These results reveal the average relative errors not exceeding 0.019%, which become smaller for the longer distances.

## References

- [1] A. E. H. Love, *A Treatise on the Mathematical Theory of Elasticity*, 2nd edn. (Cambridge University Press, Cambridge, 1906).
- [2] N. R. Keskar and J. R. Chelikowsky, *Nature* **358**, 222 (1992).
- [3] A. Yeganeh-Haeri, D. J. Weidner, and J. B. Parise, *Science* **257**, 650 (1992).
- [4] R. H. Baughman, J. M. Shacklette, A. A. Zakhidov, and S. Stafström, *Nature* **392**, 362 (1998).
- [5] J. N. Grima, R. Jackson, A. Alderson, and K. E. Evans, *Adv. Mater.* **12**, 1912 (2000).
- [6] J. N. Grima, R. Gatt, A. Alderson, and K. E. Evans, *Mater. Sci. Eng. A* **423**, 219 (2006).
- [7] R. Lakes, *Science* **235**, 1038 (1987).
- [8] K. E. Evans, M. A. Nkansah, I. J. Hutchinson, and S. C. Rogers, *Nature* **353**, 124 (1991).
- [9] M. Shokri Rad, Y. Prawoto, and Z. Ahmad, *Mech. Mater.* **74**, 76 (2014).
- [10] B. D. Caddock and K. E. Evans, *J. Phys. D, Appl. Phys.* **22**, 1877 (1989).
- [11] K. E. Evans, *J. Phys. D, Appl. Phys.* **22**, 1870 (1989).
- [12] N. Gaspar, C. W. Smith, A. Alderson, J. N. Grima, and K. E. Evans, *J. Mater. Sci.* **46**, 372 (2010).
- [13] K. W. Wojciechowski and A. C. Brańka, *Phys. Rev. A* **40**, 7222 (1989).
- [14] D. Prall and R. S. Lakes, *Int. J. Mech. Sci.* **39**, 305 (1997).
- [15] H. Abramovitch, M. Burgard, L. Edery-Azulay, K. E. Evans, M. Hoffmeister, W. Miller, F. Scarpa, C. W. Smith, and K. F. Tee, *Compos. Sci. Technol.* **70**, 1072 (2010).
- [16] P. Bettini, A. Airoidi, G. Sala, L. D. Landro, M. Ruzzene, and A. Spadoni, *Composites B* **41**, 133 (2010).
- [17] A. Spadoni and M. Ruzzene, *J. Mech. Phys. Solids* **60**, 156 (2012).
- [18] D. Attard, E. Manicaro, R. Gatt, and J. N. Grima, *Phys. Status Solidi B* **246**, 2045 (2009).
- [19] D. Attard, E. Manicaro, and J. N. Grima, *Phys. Status Solidi B* **246**, 2033 (2009).
- [20] J. N. Grima, E. Chetcuti, E. Manicaro, D. Attard, M. Camilleri, R. Gatt, K. E. Evans, and R. Proc., *Proc. R. Soc. Lond. B* **468**, 810 (2011).
- [21] J. N. Grima, E. Manicaro, and D. Attard, *Proc. R. Soc. Lond. B* **467**, 439 (2010).
- [22] D. Attard and J. N. Grima, *Phys. Status Solidi B* **249**, 1330 (2012).
- [23] N. Ravirala, A. Alderson and K. L. Alderson, *J. Mater. Sci.* **42**, 7433 (2007).
- [24] R. J. Bathurst and L. Rothenburg, *Int. J. Eng. Sci.* **26**, 373 (1988).
- [25] N. Gaspar, *Mech. Mater.* **42**, 673 (2010).
- [26] I. Shufrin, E. Pasternak, and A. V. Dyskin, *Int. J. Solids Struct.* **49**, 2239 (2012).
- [27] K. W. Wojciechowski, *Phys. Lett.* **137**, 60 (1989).
- [28] A. C. Brańka, D. M. Heyes, and K. W. Wojciechowski, *Phys. Status Solidi B* **246**, 2063 (2009).
- [29] K. V. Tretyakov, *J. Non-Cryst. Solids* **355**, 1435 (2009).
- [30] J. W. Narojczyk and K. W. Wojciechowski, *J. Non-Cryst. Solids* **356**, 2026 (2010).
- [31] A. C. Brańka, D. M. Heyes, and K. W. Wojciechowski, *Phys. Status Solidi B* **248**, 96 (2011).
- [32] A. C. Brańka, D. M. Heyes, S. Maćkowiak, S. Pieprzyk, and K. W. Wojciechowski, *Phys. Status Solidi B* **249**, 1373 (2012).
- [33] J. W. Narojczyk, P. M. Pięłowski, K. W. Wojciechowski, and K. V. Tretyakov, *Phys. Status Solidi B* **252**, 1508 (2015).
- [34] J. N. Grima, N. Ravirala, R. Galea, B. Ellul, D. Attard, R. Gatt, A. Alderson, J. Rasburn, and K. E. Evans, *Phys. Status Solidi B* **248**, 117 (2011).
- [35] C. W. Smith, J. N. Grima, and K. E. Evans, *Acta Mater.* **48**, 4349 (2000).
- [36] J. N. Grima, R. Gatt, B. Ellul, and E. Chetcuti, *J. Non-Cryst. Solids* **356**, 1980 (2010).
- [37] M. Taylor, L. Francesconi, M. Gerendás, A. Shanian, C. Carson, and K. Bertoldi, *Adv. Mater.* **26**, 2365 (2014).
- [38] L. Mizzi, K. M. Azzopardi, D. Attard, J. N. Grima, and R. Gatt, *Phys. Status Solidi RRL* **9**, 425 (2015).
- [39] A. Slann, W. White, F. Scarpa, K. Boba, and I. Farrow, *Phys. Status Solidi B* **252**, 1533 (2015).
- [40] S. Shan, S. H. Kang, Z. Zhao, L. Fang, and K. Bertoldi, *Extreme Mech. Lett.* **4**, 96 (2015).
- [41] E. Pasternak and A. V. Dyskin, *Int. J. Eng. Sci.* **52**, 103 (2012).
- [42] J. N. Grima, R. Caruana-Gauci, D. Attard, and R. Gatt, *Proc. R. Soc. Lond. B* **468**, 3121 (2012).
- [43] A. A. Pozniak, J. Smardzewski, and K. W. Wojciechowski, *Smart Mater. Struct.* **22**, 084009 (2013).
- [44] G. W. Milton, *J. Mech. Phys. Solids* **61**, 1543 (2013).
- [45] G. W. Milton, *J. Mech. Phys. Solids* **40**, 1105 (1992).
- [46] N. Phan-Thien and B. L. Karihaloo, *J. Appl. Mech.* **61**, 1001 (1994).
- [47] L. Jiang, B. Gu and H. Hu, *Compos. Struct.* **135**, 23 (2016).
- [48] I. Shufrin, E. Pasternak, and A. V. Dyskin, *Int. J. Solids Struct.* **54**, 192 (2015).
- [49] A. Bezazi and F. Scarpa, *Int. J. Fatigue* **31**, 488 (2009).
- [50] M. Bianchi, F. Scarpa, C. W. Smith, and G. R. Whittell, *J. Mater. Sci.* **45**, 341 (2009).
- [51] J. N. Grima, D. Attard, R. Gatt, and R. N. Cassar, *Adv. Eng. Mater.* **11**, 533 (2009).
- [52] M. Bianchi, S. Frontoni, F. Scarpa, and C. W. Smith, *Phys. Status Solidi B* **248**, 30 (2011).
- [53] K. Alderson, A. Alderson, N. Ravirala, V. Simkins, and P. Davies, *Phys. Status Solidi B* **249**, 1315 (2012).
- [54] B. Xu, F. Arias, S. T. Brittain, X. M. Zhao, B. Grzybowski, S. Torquato, and G. M. Whitesides, *Adv. Mater.* **11**, 1186 (1999).
- [55] H. Mitschke, J. Schwerdtfeger, F. Schury, M. Stingl, C. Körner, R. F. Singer, V. Robins, K. Mecke, and G. E. Schröder-Turk, *Adv. Mater.* **23**, 2669 (2011).
- [56] J. Schwerdtfeger, F. Schury, M. Stingl, F. Wein, R. F. Singer, and C. Körner, *Phys. Status Solidi B* **249**, 1347 (2012).
- [57] D. Y. Fozdar, P. Soman, J. W. Lee, L. H. Han, and S. Chen, *Adv. Funct. Mater.* **21**, 2712 (2011).

- [58] T. Buckmann, N. Stenger, M. Kadic, J. Kaschke, A. Frolich, T. Kennerknecht, C. Eberl, M. Thiel, and M. Wegener, *Adv. Mater.* **24**, 2710 (2012).
- [59] W. Miller, P. B. Hook, C. W. Smith, X. Wang, and K. E. Evans, *Compos. Sci. Technol.* **69**, 651 (2009).
- [60] Y. Hou, R. Neville, F. Scarpa, C. Remillat, B. Gu, and M. Ruzzene, *Composites B* **59**, 33 (2014).
- [61] P. Subramani, S. Rana, D. V. Oliveira, R. Figueiro, and J. Xavier, *Mater. Des.* **61**, 286 (2014).
- [62] G. N. Greaves, A. L. Greer, R. S. Lakes, and T. Rouxel, *Nature Mater.* **10**, 823 (2011).
- [63] Y. Prawoto, *Comput. Mater. Sci.* **58**, 140 (2012).
- [64] V. H. Carneiro, J. Meireles, and H. Puga, *Mater. Sci. Poland* **31**, 561 (2013).
- [65] T.-C. Lim, *Auxetic Materials and Structures* (Springer, Singapore, 2015).
- [66] A. Alderson and K. L. Alderson, *Proc. Inst. Mech. Eng., Part G: J. Aerospace Eng.* **565**, 221 (2007).
- [67] E. Pasternak, I. Shufrin, and A. V. Dyskin, *Compos. Struct.* **138**, 313 (2016).
- [68] K. E. Evans and A. Alderson, *Adv. Mater.* **12**, 617 (2000).
- [69] V. L. Coenen and K. L. Alderson, *Phys. Status Solidi B* **248**, 66 (2011).
- [70] I. I. Argatov, R. Guinovart-Díaz, and F. J. Sabina, *Int. J. Eng. Sci.* **54**, 42 (2012).
- [71] V. R. Simkins, A. Alderson, P. J. Davies, and K. L. Alderson, *J. Mater. Sci.* **40**, 4355 (2005).
- [72] M. Bianchi, F. Scarpa, and C. W. Smith, *Acta Mater.* **58**, 858 (2010).
- [73] Y. J. Chen, F. Scarpa, I. R. Farrow, Y. J. Liu, and J. S. Leng, *Smart Mater. Struct.* **22**, 045005 (2013).
- [74] M. N. Ali and I. U. Rehman, *J. Mater. Sci.: Mater. Med.* **22**, 2573 (2011).
- [75] K. Alderson, A. Alderson, S. Anand, V. Simkins, S. Nazare, and N. Ravirala, *Phys. Status Solidi B* **249**, 1322 (2012).
- [76] S. Jacobs, C. Coconnier, D. DiMaio, F. Scarpa, M. Toso, and J. Martinez, *Smart Mater. Struct.* **21**, 075013 (2012).
- [77] J. N. Grima, M. Caruana-Gauci, M. R. Dudek, K. W. Wojciechowski, and R. Gatt, *Smart Mater. Struct.* **22**, 084016 (2013).
- [78] R. Brighenti, *Thin-Walled Struct.* **84**, 432 (2014).
- [79] I. Shufrin, E. Pasternak, and A. V. Dyskin, *Int. J. Eng. Sci.* **89**, 100 (2015).
- [80] E. Pasternak, A. V. Dyskin, and I. Shufrin, in: *Proc. 6th Australasian Congress on Applied Mechanics (ACAM 6)*, Perth, Australia, 2010, p. 1266.
- [81] L. Rothenburg, A. A. Berlin, and R. J. Bathurst, *Nature* **354**, 470 (1991).
- [82] E. Pasternak and H. Mühlhaus, in: *Computational Mechanics—New Frontiers for New Millennium*, edited by S. Valliappan and N. Khalili, Vol. 2 (Elsevier Science, Amsterdam, 2001), p. 1189.
- [83] E. Pasternak, H. B. Mühlhaus, and A. V. Dyskin, *Pure Appl. Geophys.* **161**, 2309 (2004).
- [84] E. Pasternak and H. B. Mühlhaus, *J. Eng. Math.* **52**, 199 (2005).
- [85] E. Pasternak and A. V. Dyskin, in: *IUTAM Symposium on Scaling in Solid Mechanics* (Springer, Heidelberg, 2008), pp. 49–58.
- [86] L. D. Landau, E. M. Lifshitz, A. M. Kosevich, and L. P. Pitaevskii, *Theory of Elasticity*, 3rd edn. (Butterworth-Heinemann, Oxford, 1986).
- [87] A. Dunn, Homogenisation by differential expansions and determination of Cosserat moduli for specially constructed granulate materials (supervised by E. Pasternak and A.V. Dyskin A.V.), The University of Western Australia, 2008.
- [88] E. Pasternak and A. V. Dyskin, in: *Mechanics of Generalized Continua: One Hundred Years After the Cosserats*, edited by G. Maugin and A. Metrikine (Springer, New York, 2010), pp. 71–78.
- [89] E. Pasternak and A.V. Dyskin, Reconstruction of Cosserat moduli in particulate materials, in: *9th HSTAM (Hellenic Society for Theoretical and Applied Mechanics) International Congress on Mechanics*, edited by P. Papanastasiou, E. Papamichos, A. Zervos, and M. Stavropoulou, *Proceedings of Vardoulakis mini-symposia – Higher Order Continua*, Limassol, Cyprus, 12–14 July, 2010, pp. 69–75.
- [90] E. Pasternak and A. V. Dyskin, *Acta Mech.* **225**, 2409 (2014).
- [91] E. Pasternak, A. V. Dyskin, M. Esin, G. M. Hassan, and C. MacNish, *Philos. Mag.* **28–30**, 3122 (2015).
- [92] W. Nowacki, *Theory of Micropolar Elasticity* (Springer-Verlag, Wien, 1970).
- [93] W. Weaver and J. M. Gere, *Matrix Analysis of Framed Structures*, 3rd edn. (Kluwer Academic Publishers, Netherlands, 1990).
- [94] T. Luhmann, S. Robson, S. Kyle, and I. Harley, *Close Range Photogrammetry: Principles, Methods and Applications* (Whittles Publishing, Dunbeath, 2006).
- [95] C. S. Fraser, *Photogramm. Eng. Remote Sens.* **58**, 305 (1992).
- [96] C. S. Fraser, A. Woods, and D. Brizzi, *Photogramm. Record.* **20**, 205 (2005).
- [97] T. Luhmann, *ISPRS J. Photogramm. Remote Sens.* **65**, 558 (2010).
- [98] S. Franke, B. Franke, and K. Rautenstrauch, *Mater. Struct.* **40**, 37 (2006).
- [99] R. Jiang, D. V. Jáuregui, and K. R. White, *Measurement* **41**, 823 (2008).
- [100] T. K. Lee and R. Al-Mahaidi, *Compos. Struct.* **82**, 185 (2008).
- [101] J. Ye, G. Fu, and U. P. Poudel, *J. Eng. Mech.* **137**, 475 (2011).
- [102] X. Qi, D. D. Lichti, M. El-Badry, T. O. Chan, S. I. El-Halawany, H. Lahamy, and J. Steward, *Photogramm. Record.* **29**, 89 (2014).
- [103] T. G. Ryall and C. S. Fraser, *J. Aircraft* **39**, 114 (2002).
- [104] M. R. Bambach, *Thin-Walled Struct.* **47**, 485 (2009).
- [105] C. S. Fraser and B. Riedel, *ISPRS J. Photogramm. Remote Sens.* **50**, 268 (2000).
- [106] J. Valença, D. Dias-da-Costa, and E. N. B. S. Júlio, *Constr. Build. Mater.* **28**, 607 (2012).
- [107] J. Valença, D. Dias-da-Costa, E. Júlio, H. Araújo, and H. Costa, *Measurement* **46**, 433 (2013).
- [108] C. S. Fraser and S. Cronk, *ISPRS J. Photogramm. Remote Sens.* **64**, 328 (2009).
- [109] Photometrix, at: [www.photometrix.com.au](http://www.photometrix.com.au) (2015).
- [110] S. Cronk, C. Fraser, and H. Hanley, *Photogramm. Record.* **21**, 355 (2006).
- [111] C. Stamatopoulos and C. S. Fraser, *Photogramm. Record.* **26**, 339 (2011).
- [112] M. Eisenberger, *Comput. Struct.* **40**, 831 (1991).
- [113] S. P. Timoshenko and J. N. Goodier, *Theory of Elasticity* (McGraw-Hill Book Co., Singapore, 1982).